FULL PAPER

All-Carbon Nanoarchitectures as High-Performance Separation Membranes with Superior Stability

Kunli Goh, Wenchao Jiang, Huseyin Enis Karahan, Shengli Zhai, Li Wei, Dingshan Yu, Anthony G. Fane, Rong Wang, and Yuan Chen**

The application of graphene-based membranes is hindered by their poor stability under practical hydrodynamic conditions. Here, nanocarbon architectures are designed by intercalating surface-functionalized, small-diameter, multi-walled carbon nanotubes (MWCNTs) into reduced graphene oxide (rGO) sheets to create highly stable membranes with improved water permeability and enhanced membrane selectivity. With the intercalation of 10 nm diameter MWCNTs, the water permeability reaches 52.7 L m^{-2} h^{-1} bar^{-1}, which is 4.8 times that of pristine rGO membrane and five to ten times higher than most commercial nanofiltration membranes. The membrane also attains almost 100% rejection for three organic dyes of different charges. More importantly, the membrane can endure a turbulent hydrodynamic flow with cross-flow rates up to 2000 mL min^{-1} and a Reynolds number of 4667. Physicochemical characterization reveals that the inner graphitic walls of the MWCNTs can serve as spacers, while nanoscale rGO foliates on the outer walls interconnect with the assimilated rGO sheets to instill superior membrane stability. In contrast, intercalating with single-walled nanotubes fails to reproduce such stability. Overall, this nanoarchitectured design is highly versatile in creating both graphene-rich and CNT-rich all-carbon membranes with engineered nanochannels, and is regarded as a general approach in obtaining stable membranes for realizing practical applications of graphene-based membranes.

1. Introduction

Membrane-based separation plays a critical role in meeting today's water treatment challenges[1] because of its numerous advantages such as energy efficiency, cost effectiveness, and reduced carbon footprints.[2] As such, constant efforts have been placed on fabricating novel membranes which can provide high throughput, high selectivity, and good membrane stability.[2,3] Sp^2-hybridized carbon nanomaterials, such as graphene and carbon nanotubes (CNTs), have shown great potential as membranes for separation processes, owing to their unique water transport properties[4] and excellent molecular sieving capabilities.[5]

In particular, graphene oxide (GO), with its 2D structure and tunable nanopores or nanochannels,[6] has attracted the interest of many researchers to fabricate GO based novel membranes. However, the GO membranes fabricated so far often suffer from poor stability under practical hydrodynamic flow conditions[7] because the presence of hydrophilic oxygen-containing functional groups and negative charges on the GO sheets result in undesirable redispersion of the membranes when hydrated.[8] To circumvent this issue, a recent study has reported the chemical reduction of GO membrane to reduced graphene oxide (rGO) membrane using hydroiodic acid. Due to the removal of the oxygen-containing functional groups from the GO sheets, rGO membrane has a more compacted lamellar structure and exhibits much better membrane stability in water.[9] Unfortunately, the water permeability of such membrane decreases drastically due to the higher hydrodynamic resistance of the narrower interlayer spacing between the rGO sheets.[10] Another recent study has also shown that multivalent cationic metal contaminants (primarily Al^{3+} and Mn^{2+}), which are unintentionally introduced during GO membrane processing, can act as effectively cross-linkers to improve the stability of the GO membrane in water.[11] Nevertheless, new methods are urgently needed to fabricate graphene-based membranes with both high throughput and membrane stability for realizing their practical applications.

In this work, we describe the development of all-carbon nanoarchitectures comprising of rGO sheets and multi-walled carbon nanotubes (MWCNTs) as high performance separation membranes with superior stability. GO sheets were first amalgamated

K. Goh
Interdisciplinary Graduate School
Nanyang Technological University
Singapore 639798, Singapore
K. Goh, Prof. A. G. Fane, Prof. R. Wang
Singapore Membrane Technology Center
Nanyang Environment and Water Research Institute
Nanyang Technological University
Singapore 637141, Singapore
E-mail: rwang@ntu.edu.sg
K. Goh, W. Jiang, H. E. Karahan, S. Zhai, Dr. L. Wei, Prof. Y. Chen
School of Chemical and Biomedical Engineering
Nanyang Technological University
Singapore 637459, Singapore
E-mail: chenyuan@ntu.edu.sg
Prof. D. Yu
Key Laboratory for Polymeric Composite and Functional Materials of Ministry of Education
School of Chemistry and Chemical Engineering
Sun Yat-sen University
Guangzhou 510275, P. R. China

DOI: 10.1002/adfm.201502955

with surface functionalized MWCNTs in different amounts and the membranes were fabricated via a filtration process. The ensuing membranes were then chemically reduced to create different all-carbon nanoarchitectures. By doing so, we take advantage of the following synergistic effects. First, the intercalation of MWCNTs between adjacent rGO sheets can effectively inhibit the restacking (or aggregation) of the rGO sheets and thus create nanochannels for water transport. Second, the nanochannels created can be engineered using MWCNTs of different diameters so as to retain the molecular sieving capability of the ensuing membranes. Third, MWCNTs can also act as anchors to interact and interconnect with the adjacent rGO sheets so as to reinforce the membrane stability. The effects of MWCNT intercalation on the water permeability and molecular sieving capability of the membranes are then systematically studied together with the detailed physicochemical characterization of these membranes. Most importantly, the stability of these all-carbon nanoarchitectured membranes is assessed for the first time by subjecting the membranes to varying cross-flow rates of different hydrodynamic flow conditions. This is in contrast to previous studies where membrane stability was typically evaluated by just submerging the membranes in stagnant water.[12] In addition, the mechanistic understanding of the membrane stability of these all-carbon nanoarchitectured membranes is also elucidated.

2. Results and Discussion

2.1. Fabrication of All-Carbon Nanoarchitectured Membranes

We initially fabricated an ultrathin GO membrane via pressure-assisted filtration and subsequently reduced it using 57 wt% HI acid to obtain a pristine rGO membrane as illustrated in **Figure 1**a. MWCNTs were then intercalated between the GO sheets before the reduction step (Figure 1b) to create nanoarchitectured membranes in order to mitigate the drop in water permeability brought by the decreased in the interlayer spacing due to the HI reduction.[4c] The intercalated MWCNTs can inhibit the restacking of the rGO sheets and create nanochannels to facilitate water transport through the ultrathin rGO membranes. Depending on the amount of MWCNTs intercalated, the morphology of these membranes can be easily tuned into two different types, namely, graphene-rich and CNT-rich nanoarchitectures (Figure 1b). This all-carbon nanoarchitecture design arises from the following rationales. First, a pressure-assisted filtration process can be employed to yield a tight GO laminate with highly ordered microstructure as reported by Tsou et al.[13] Second, HI is chosen over other reducing agents such as hydrazine as it helps to maintain structural integrity of the GO laminate by providing a gentle chemical reduction which produces water instead of CO and CO_2 gases. The water is believed to travel along the capillaries between the GO sheets without inflicting damage to the microstructure.[10] An alternative approach to minimize defects in the GO membrane is to increase its thickness. However, two major drawbacks to this approach are the exponential decrease in the water permeability (Figure S1, Supporting Information) and the lack of improved membrane stability as membrane thickness increased. As such, we adopted this ultrathin membrane design to reduce hydrodynamic resistance and made deliberate considerations over the filtration process and the reducing agent to enhance the stability of the ultrathin membrane. Third, MWCNTs are chosen to create the nanochannels for water transport in virtue of their high aspect ratios, excellent strength, and smooth hydrophobic

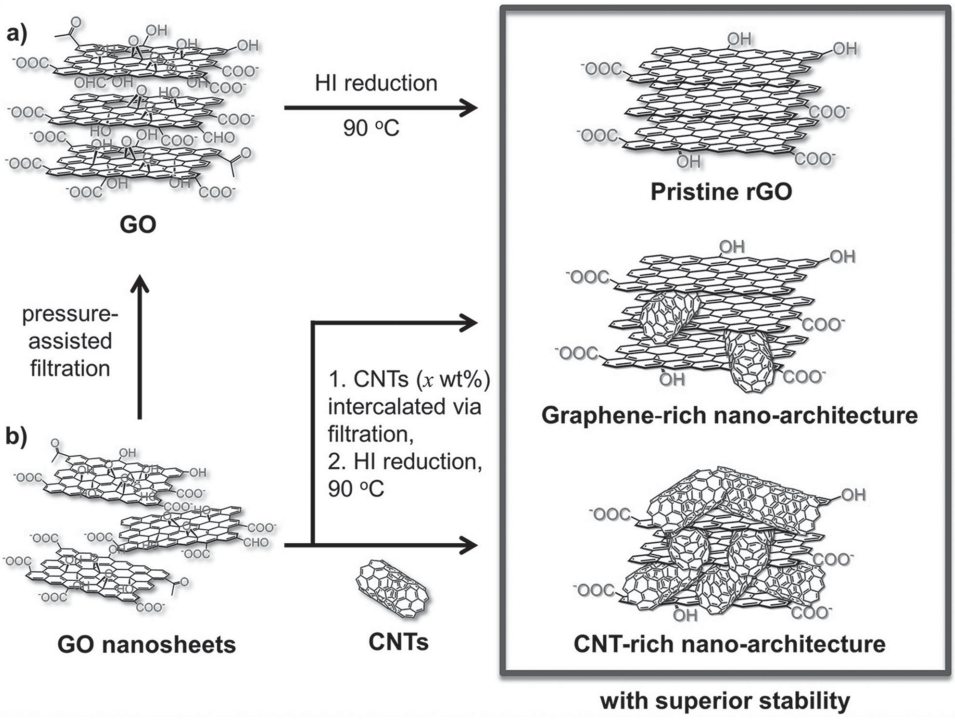

Figure 1. Schematic illustrations of the fabrication process leading to a) aultrathin rGO membranes and b) all-carbon nanoarchitectured membranes.

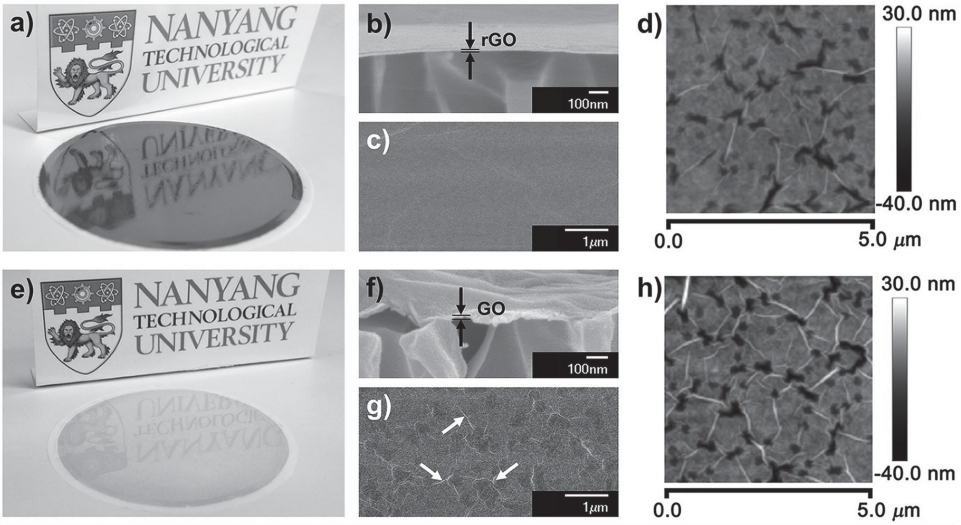

Figure 2. a) Photography of the pristine rGO membrane showing the reflective metallic luster, FE-SEM images of the b) cross-sectional view and c) surface morphology of the pristine rGO membrane, d) AFM image showing the topography of the pristine rGO membrane. e) Photography of the GO membrane showing less reflective luster. FE-SEM images of the f) cross-sectional and g) surface morphology of the GO membrane with more wrinkles as highlighted by the white arrows, and h) AFM image showing the topography of the GO membrane.

graphitic walls.[14] Overall, all these factors come together to ensure the formation of tight and stable all-carbon nanoarchitectures with high water permeability and minimal structural defects.

As shown in **Figure 2**a, the as-prepared ultrathin pristine rGO membrane exhibits a smooth surface with a mirror-like finishing. This suggests that a highly ordered laminate structure is formed and the structural integrity is well preserved during the reduction process. The rGO membrane is estimated to be ≈55 ± 3 nm in thickness (Figure 2b and Figure S2a, Supporting Information) while the outer surface of the rGO membrane appears smooth and reveals minimal wrinkles as depicted by the field emission-scanning electron microscopic (FE-SEM) and atomic force microscopic (AFM) images, respectively (Figure 2c,d). In contrary, the as-prepared ultrathin GO membrane lack the mirror-like finishing despite exhibiting a smooth surface (Figure 2e). The GO membrane is also slightly thicker at ≈90 ± 5 nm (Figure 2f and Figure S2b, Supporting Information) and reveals more wrinkles (Figure 2g,h). Due to the presence of these wrinkles, the surface roughness of the GO membrane is higher at 8.29 ± 0.96 nm as compared to the rGO membrane at 5.62 ± 0.95 nm (Figure S2c,d, Supporting Information). Such wrinkles in the GO membrane arise from the hydrogen bonding between the hydrophilic functional groups on the basal planes and edges of the GO sheets. This hydrogen bonding affects how the convoluted GO sheets are assembled and thus contributing to the wrinkles.[15] On the other hand, the removal of these hydrophilic groups during the reduction process allows the rGO sheets to smoothen out before restacking into a less wrinkled laminate structure.

Intercalation of MWCNTs into the membrane is then explored by fabricating a series of nanoarchitectured membranes consisting of 10, 30, 50, and 80 wt% MWCNTs. To demonstrate that MWCNTs can create nanochannels of different sizes to facilitate water transport, MWCNTs of two diameters, 10 and 50 nm (Figure S3, Supporting Information), are utilized. The MWCNT intercalated membranes are designated as rGO_*x*MWCNT(*y*) where *x* represents the wt% of MWCNTs loaded and *y* represents the diameter of the MWCNT used. For example, rGO_30MWCNT(10) denotes a membrane with 30 wt% MWCNT loading using 10 nm diameter MWCNTs. As shown in **Figure 3**a–d, nanoarchitectured membranes of different MWCNT loadings all appear uniform and smooth with their colors looking darker as the MWCNT loading increases. At low MWCNT loadings (≤50 wt%), the membranes reveal a metallic gray luster (Figure 3a–c), but this luster disappears for rGO_80MWCNT(10) (Figure 3d). These observations suggest that the intercalated MWCNTs integrate well with the rGO sheets, and the structural integrity stays intact after the intercalation. However, the roughness of these membranes increases as a result of the undulating outer surfaces caused by the intercalated MWCNTs (Figure S4, Supporting Information). The cross-sectional morphologies of these membranes are also investigated via FE-SEM to elucidate their microstructures. As illustrated in Figure 3e–l, the MWCNTs are uniformly intercalated regardless of the diameters of the MWCNTs used. Further analysis of the FE-SEM images of rGO_10MWCNT(10) to rGO_80MWCNT(10) shows an increase of the membrane thickness from ≈64 ± 2 to ≈1230 ± 70 nm (Figure 3e–h). Such a dramatic change in the thickness indicates that the interlayer spacing between the rGO sheets has been immensely disrupted by the intercalated MWCNTs. Interestingly, the change in thickness of the membrane is not as radical when 50 nm diameter MWCNTs are loaded. The thickness of rGO_10MWCNT(50) to rGO_50MWCNT(50) is largely similar to their 10 nm MWCNT counterparts (Figure 3i–k) except for rGO_80MWCNT(50) which has a thickness of ≈570 ± 18 nm (Figure 3l). This is at least two times smaller than the membrane thickness of rGO_80MWCNT(10). While this observation seems counterintuitive initially, it can be rationalized by studying the mass difference between the 10 and 50 nm diameter MWCNTs. Transmission electron microscopic (TEM) analysis of the MWCNTs

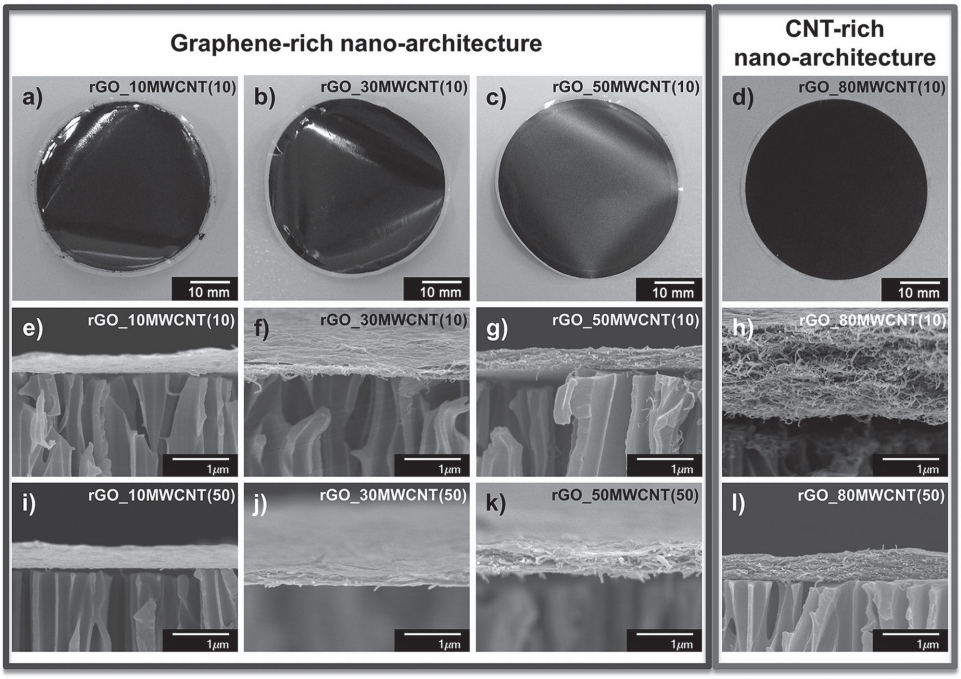

Figure 3. a–d) Photographies and e–h) cross-sectional FE-SEM images of the all-carbon nanoarchitectured membranes with 10 nm diameter MWCNTs intercalated; i–l) cross-sectional FE-SEM images of the all-carbon nanoarchitectured membranes with 50 nm diameter MWCNTs intercalated.

($n > 100$) reveals that the inner diameter of the 50 nm diameter MWCNTs is similar to that of the 10 nm MWCNTs and thus the number of graphitic walls possessed by the 50 nm diameter MWCNTs is significantly more (Figure S3, Supporting Information). By estimating the number of walls and conducting a simple calculation (Supporting Information),[16] the mass of a 50 nm diameter MWCNT is found to be at least 15 times heavier than a 10 nm MWCNT. This means that, for the same mass of MWCNTs loaded, the number of 50 nm diameter MWCNTs intercalated into the rGO membrane is significantly lower than that of the 10 nm MWCNTs, resulting in a weaker disruption of the interlayer spacing between the rGO sheets. This, in turn, induces a tighter membrane packing density and hence a smaller membrane thickness of rGO_80MWCNT(50). Such a phenomenon is only observable when the MWCNT loading exceeds 50 wt%, which suggests that the architecture of the membrane changes beyond this loading. As such, we term these two architectures as graphene-rich and CNT-rich when the MWCNT loadings are below and above 50 wt%, respectively (Figure 3).

2.2. Separation Performances of All-Carbon Nanoarchitectured Membranes

The water permeability (L m^{-2} h^{-1}) of the respective membranes are evaluated under 1 bar pressure and represented as water permeability coefficients (L m^{-2} h^{-1} bar^{-1}) while the separation performances of these membranes are assessed using three different organic dye solutions, namely, methylene blue (MB), acid orange 7 (AO7), and rhodamine B (RhB). MB (319.85 g mol^{-1}) is a positively charged molecule with a dimension of 1.6 × 0.8 nm while AO7 (350.32 g mol^{-1}) has a similar dimension (1.6 × 1.0 nm) but negatively charged.[17] RhB (479.02 g mol^{-1}) is an electroneutral molecule with a larger dimension of 1.8 × 1.4 nm.[18] These solutes are deliberately chosen due to their different charges and various molecular weights so that a comprehensive understanding of the sieving mechanism can be made. The results are summarized in **Figure 4**.

As shown in Figure 4a, the water permeability coefficients of the nanoarchitectured membranes are found to increase with higher MWCNT loadings. Consequently, the hydrodynamic resistances of these membranes decrease as the MWCNT loading increases (Figure S5, Supporting Information), taking into account that the resistance brought by the rGO sheets is the same given the same amount of rGO used in every membrane. These results suggest that MWCNTs have successfully created the nanochannels among the rGO sheets for water transport. To further validate this finding, the water permeability coefficients of the nanoarchitectured membranes intercalated with 50 nm diameter MWCNTs are compared against their 10 nm MWCNT counterparts. The water permeability coefficients of those membranes with 50 nm diameter MWCNTs are higher than their 10 nm MWCNT counterparts at every MWCNT loading except for the MWCNT loading at 80 wt% (Figure 4a). These results are in good agreement with those recently reported in the literature.[12c,19] At the MWCNT loading of 80 wt%, the nanoarchitecture changes from graphene-rich to CNT-rich and thus an opposite trend is observed with rGO_80MWCNT(50) having a water permeability coefficient lower than that of rGO_80MWCNT(10). To further explain for this difference, the membrane density of the nanoarchitectured membranes was explored. The density of these membranes

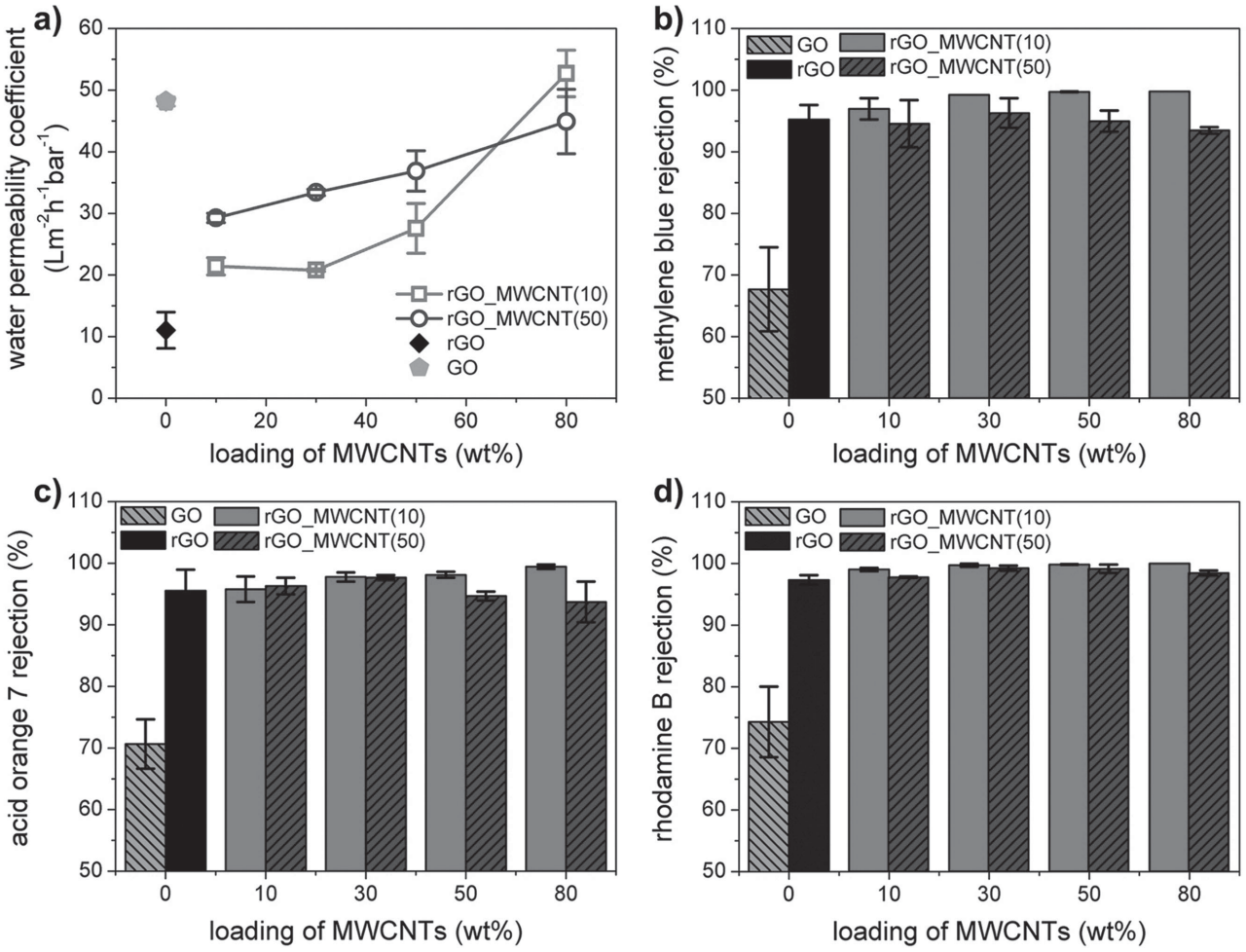

Figure 4. Separation performances showing a) water permeability coefficients and the b–d) rejection rates of MB, AO7, and RhB, respectively, for GO, rGO, and all-carbon nanoarchitectured membranes.

exhibits a linear decreasing trend up to 50 wt% MWCNT loading, with rGO_10MWCNT(50) to rGO_50MWCNT(50) having smaller densities as compared to their 10 nm MWCNT counterparts. However, at the 80 wt% MWCNT loading, the membrane density of rGO_80MWNCT(10) increases marginally while that of rGO_80MWCNT(50) increases significantly (Figure S6, Supporting Information), for the same reasons which have already been discussed in Section 2.1. This observation suggests that the nanoarchitecture of the rGO membrane with 80 wt% MWCNT loading is evidently different from the other rGO membranes of lower MWCNT loadings. It also shows that, for each distinct type of nanoarchitecture, the membrane density is inversely proportionate to the water permeability coefficient where a higher membrane density results in a lower water permeability coefficient and vice versa. In this regard, it is thus noteworthy to mention that such a shift in the nanoarchitecture as MWCNT loading increases is not only evident from the membrane morphology but also clearly manifested in the water permeability of the membrane and its microstructural parameter such as membrane density. Overall, intercalation of MWCNTs into rGO sheets has resulted in an increment of water permeability with rGO_80MWCNT(10) having a permeability up to 4.8 times that of the pristine rGO membrane.

Next, the separation performances of these membranes were evaluated. As illustrated in Figure 4b–d, the rGO membrane shows significant improvement in the rejection rates as compared to the GO membrane. With just an ultrathin rGO membrane, the rejections of the three dye solutes can generally reach rates above 95%. When 10 nm diameter MWCNTs are intercalated, the rejection rates further exceed that of the pristine rGO membrane, indicating that the 10 nm intercalated MWCNTs integrate well with the rGO sheets. For its 50 nm MWCNT counterparts, the rejection rates of these dye solutes increase slightly at low MWCNT loadings (up to 30 wt%) before dipping at higher MWCNT loadings (Figure 4b–d). Such a trend is consistent with those reported in the literature which suggests the generation of more pathways for the dye solutes to permeate due to a greater amount of 50 nm diameter MWCNTs loaded.[19] To further demonstrate that the membrane selectivity arises from the synergism of the rGO sheets and the intercalated MWCNTs, the separation performance of a pure reduced MWCNTs membrane was evaluated. Unsurprisingly, the pure reduced MWCNTs membrane exhibits a poor

selectivity with dye solute rejection rates between 5% and 20%, despite having a much higher water permeability coefficient of 2234 ± 63 L m^{-2} h^{-1} bar^{-1} (Table S1, Supporting Information). Based on this account, as with 10 nm diameter MWCNTs, it is conclusive that the seamless assimilation of MWCNTs into the rGO sheets has successfully created nanochannels to enhance water permeability and yet provide effective molecular sieving for larger solutes.

2.3. Physicochemical Characterization of Membranes and Their Separation Mechanism

In an effort to provide plausible explanations to the above membrane separation performance results, various characterizations were carried out on the membranes. The chemical states of the membranes are first examined using Raman and Fourier transformed-infrared (FT-IR) spectroscopy. As shown in **Figure 5**a, the Raman intensity ratio of the D to G band (I_D/I_G) increases from 1.2 to 1.6 when GO is reduced to rGO membrane. This confirms a successful restoration of sp^3 carbons in the GO membrane to sp^2 carbons in the rGO membrane by the HI reduction.[20] The increased I_D/I_G ratio of 1.7 observed in the spectra of both rGO_80MWCNT(10) and rGO_80MWCNT(50) and the presence of the 2D bands also indicate effective restoration to give more graphitic sp^2 carbons in both the rGO sheets and the intercalated MWCNTs.[21] These findings can be corroborated by the FT-IR results (Figure 5b). The oxygen-containing functional groups on the GO spectrum assigned as C=O (1720 cm^{-1}), C–OH (1404 cm^{-1}), and C–O (1062 cm^{-1}) stretching vibrations[22] are absent from the rGO spectrum, implying their removal during the reduction process. On the other hand, the extent of reduction is limited for the MWCNTs given the sharp OH stretching vibrations in the region of 3500–3800 cm^{-1} due to free hydroxyl groups[23] present in both oxidized and reduced MWCNTs. Coupled with the presence of the C–O (1062 cm^{-1}), asymmetric and symmetric CH_2 (2902 and 2980 cm^{-1}) stretching vibrations in the spectra of rGO_80MWCNT(10) and rGO_80MWCNT(50), we evidently infer the successful reduction of GO to rGO sheets while the intercalated MWCNTs remain largely hydrophilic in these membranes. As a result, the water contact angles of the nanoarchitectured membranes decrease with increasing MWCNT loadings as demonstrated in Figure 5c. The X-ray diffraction

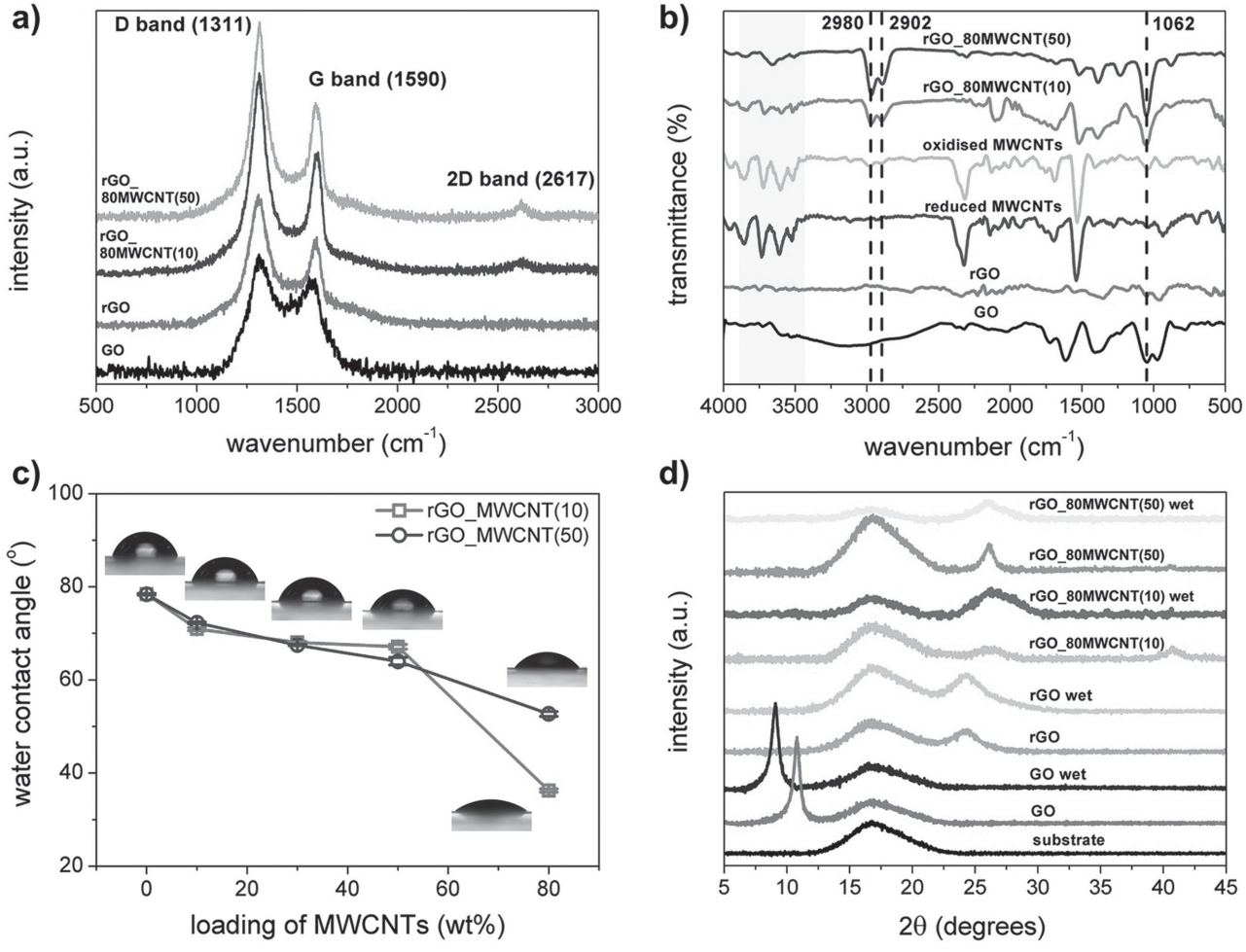

Figure 5. Physicochemical characterization as elucidated by a) Raman spectrum using a 785 nm laser, b) ATR FT-IR spectrum, c) water contact angles of the membranes at different MWCNT loadings, and d) XRD patterns of the membranes at wet and dry states.

(XRD) patterns (Figure 5d) were also analyzed to understand changes in the interlayer spacing of these membranes. A 2θ shift in the (002) peak of the GO membrane from 10.8° to 9.1° (corresponding to an increase in interlayer spacing from 0.82 to 0.97 nm) suggests that the GO membrane is highly hydrophilic and is susceptible to swelling when wetted.[24] However, upon successful HI reduction, a broad peak that appears at 24.3° (corresponding to an interlayer spacing of 0.36 nm), as a result of the removal of oxygen-containing functional groups[25] which induces partial restacking of the exfoliated rGO sheets,[26] does not produce the same shift when wetted. We attribute this to the hydrophobicity of the rGO sheets (Figure 5c) and the reduced interlayer spacing which restricts water intercalation. When 80 wt% MWCNTs are loaded, the broad peak disappears and instead MWCNTs peaks appear at 26.2° and 40.7° which correspond to the (002) and (100) planes of the hexagonal graphitic structures of MWCNTs, respectively.[27] This implies that the MWCNTs have been effectively intercalated and inhibited the restacking of the rGO sheets during the reduction process.[26]

From all these characterization results, we deduce that the intercalated MWCNTs stay hydrophilic and continue to create effective nanochannels after the HI reduction process by allowing favorable water access through their hydrophilic sites[18] and faster water permeation through the enlarged interlayer spacing between the rGO sheets.[4c] As a result, the water permeability coefficients increase with increasing MWCNT loadings (Figure 4a). When 50 nm diameter MWCNTs are intercalated, this interlayer spacing between the rGO sheets is widened to a larger extent and thus permitting greater water permeation through the graphene-rich nanoarchitectured membranes.[19]

On the other hand, the removal of oxygen-containing functional groups during the reduction process which induces restacking of the rGO sheets has rendered the pristine rGO membrane less negative electrostatic charges[28] and a narrower interlayer spacing.[4c,10] Based on these conclusions and considering negligible dye adsorption rates by the respective membranes (Table S2, Supporting Information), we propose size exclusion as the dominant sieving mechanism for the retention of the dye solutes in the pristine rGO membrane.[29] As verified by Figure 4b,c, the similar MB and AO7 rejection rates (≈95%) of the rGO membrane suggest that Donnan (charge) exclusion is not the predominant mechanism given that different charges on solutes of similar molecular weights do not seem to have an effect on their rejection rates. In fact, the slightly higher rejection rate (97.3%) of the electroneutral RhB solutes of higher molecular weight (Figure 4d) validated this deduction. These results thus demonstrate that the pristine rGO membrane has a molecular weight cutoff between the range of 200 to 2000 Da which classifies it as a nanofiltration (NF) membrane.[12a,30] Microstructural defects created during the restacking of the rGO sheets dismiss the possibility of absolute exclusion of the dye solutes which theoretically should be anticipated given a relatively smaller interlayer spacing of 0.36 nm between the rGO sheets as compared to the larger dimensions of the solutes.[31]

The exact same trends in the rejection rates are also observed when MWCNTs are intercalated. Rejection rates of MB, AO7, and RhB, respectively, increase to 99.8%, 99.4%, and 100% for rGO_80MWCNT(10) and 96.3%, 97.7%, and 99.2% for rGO_30MWCNT(50) as depicted in Figure 4b–d. The increase in the rejection rates of the higher molecular weight RhB solutes again brought us to the same conclusion that size as opposed to Donnan exclusion is the predominant sieving mechanism. More evidence to support this conclusion is also demonstrated through the pore size distributions of these membranes (Figure S7, Supporting Information). Assuming that the interlayer spacing between the rGO sheets is equivalent to a cylindrical pore with a circular cross-section, the mean pore diameters of rGO_10MWCNT(10) to rGO_80MWCNT(10) are found to be around 0.96 nm while their 50 nm MWCNT counterparts show an increasing mean diameter from 1.10 to 1.29 nm with increasing MWCNT loadings (Figure S7b,c, Supporting Information). This means that the all-carbon nanoarchitectured membranes can effectively block out the evaluated dye solutes which are larger in dimensions. In addition, the highly tapered pore size distribution of rGO_80MWCNT(10), in contrast to the broader distributions of the other nanoarchitectured membranes, accounts for the higher membrane selectivity of rGO_80MWCNT(10). As a result of these two factors, rGO_80MWCNT(10) can achieve almost 100% rejection rates which is unattainable at the same wt% loading when 50 nm diameter MWCNTs are loaded instead.

Essentially, the characterization and separation performance results have shown that the water permeability of the membrane is dependent on its membrane density while the membrane selectivity is closely related to the diameter of the MWCNTs loaded. With this understanding, synergism can then be fostered through assimilating a high loading of MWCNTs into the rGO sheets to immensely disrupt the interlayer spacing and create nanochannels to facilitate water permeation while the employment of small diameter MWCNTs to constrict these nanochannels effectively leads to smaller membrane pore size that can enhance size exclusion effect and hence the membrane selectivity.

2.4. Stability of Membranes and the Mechanism

Membrane stability was systematically studied under various cross-flow conditions using the ultrathin pristine rGO membrane and a representative from each type of the nanoarchitecture, namely, rGO_80MWCNT(10) and rGO_50MWCNT(10). The membranes, with an effective surface area of 4.5 cm^2, are first potted into an in-house made cross-flow testing cell before subjected to cross-flow rates of 500, 1000, and 2000 mL min^{-1} to evaluate their stability. These cross-flow rates are equivalent to cross-flow velocities of 0.55, 1.11, and 2.22 m s^{-1} and Reynolds numbers (R_e) of 1167, 2333, and 4667, respectively. The rates are chosen to create varying flow conditions ranging from laminar, transition to turbulent flow. Ultrathin GO membrane with the same GO loading as the pristine rGO membrane is also subjected to cross-flow rates up to 500 mL min^{-1} as a control.

As demonstrated in Video S1 (Supporting Information), the pristine rGO membranes, rGO_80MWCNT(10) and rGO_50MWCNT(10), exhibit excellent stability when subjected to different flow conditions. These membranes were initially evaluated under a moderate 500 mL min^{-1} cross-flow

rate which created a laminar flow that exerted a shear stress of 0.98 N m^{-2} on the surfaces of the membranes (Supporting Information). The membranes managed the flow and stress well without incurring any visible damage as they were compressed. Air bubbles were intermittently allowed in to provide an indication of the cross-flow rates. Next, the membranes were subjected to higher cross-flow rates of 1000 and 2000 mL min^{-1}. Similarly, the membranes handled the change in the fluid dynamics with ease as the flow transited from laminar to transitional and finally to turbulent. Stronger shear stress due to the increased cross-flow rates further compressed the membranes. As the turbulent flow and shear stress were alleviated by returning the cross-flow rate back to 40 mL min^{-1}, all the membranes loosened up without a glitch as shown in **Figure 6**a–f. To further validate such membrane stability, a long term stability evaluation is performed on rGO_80MWCNT(10). The membrane displayed excellent durability when subjected to a cross-flow rate of 500 mL min^{-1} over a duration of 24 h. No compromise on the integrity of the membrane was visible after the evaluation (Figure S8, Supporting Information), which again demonstrated the excellent membrane stability.

To highlight the disparity in the membrane stability, an ultrathin GO membrane is put to the test. As revealed in Video S2 (Supporting Information), the GO membrane started to peel off from the polycarbonate (PC) substrate at a relatively low cross-flow rate of 100 mL min^{-1}. This rate is equivalent to a cross-flow velocity of 0.11 m s^{-1} and a R_e of 233. At a higher cross-flow rate of 500 mL min^{-1}, fragmented GO platelets were also found to be carried away by the cross-flow. These observations suggest that the ultrathin GO membrane is highly unstable and is incapable of withstanding a shear stress as low as 0.2 N m^{-2}. We attribute this to its hydrophilicity which allows the oxygen-containing functional groups on the GO sheets to form strong hydrogen bonding with the water shearing on the membrane surface.[8,11] As a result, the shear stress is able to rupture the GO membrane as shown in Figure 6g,h.

On the basis of these experimental results, a mechanism is then proposed to explain for the good membrane stability of the pristine rGO and the nanoarchitectured membranes. As already discussed, oxygen-containing functional groups on the GO membrane induce hydrophilic interactions with water and make the membrane susceptible to water intercalation. Therefore, our strategy revolves around the removal of these oxygen-containing functional groups in the pristine rGO membrane, which not only makes its surface hydrophobic but increases the van der Waals attractions and π–π stacking interactions between the rGO sheets.[14b,32] As a result, the interlayer spacing between the rGO sheets decreases, preventing water intercalation and thus swelling and redispersion of the pristine rGO membrane. Explanations as such have been widely accepted as the reasons for rGO stability in water.[8,9,11]

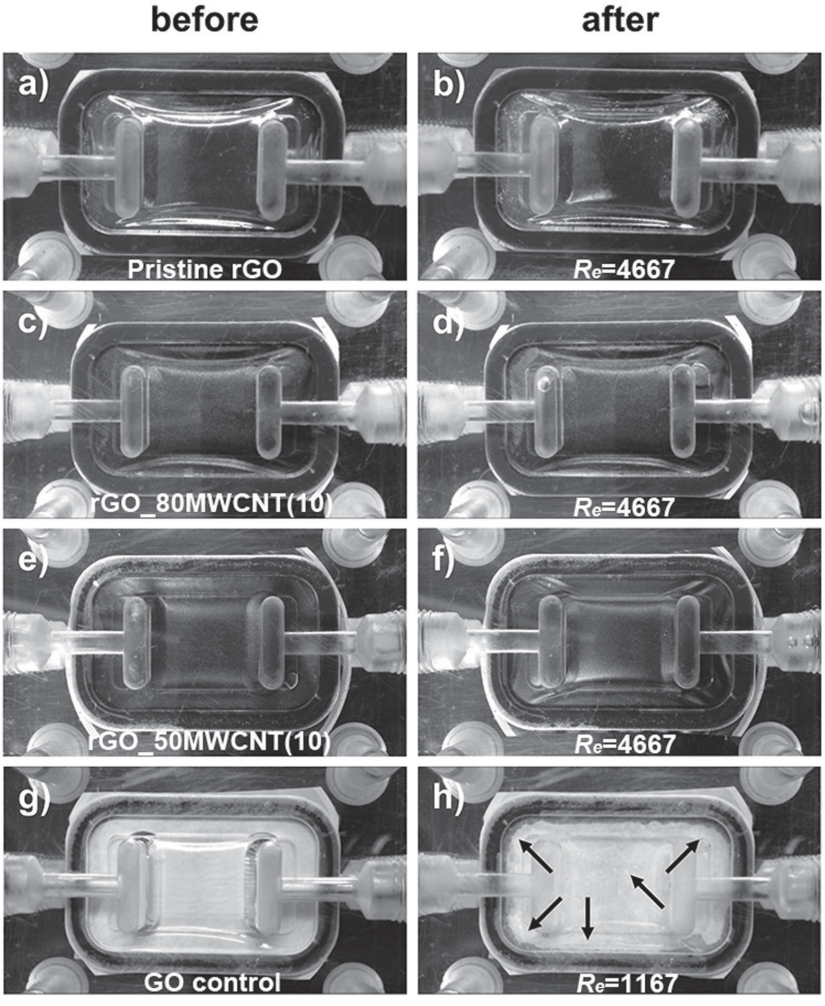

Figure 6. Photos showing the membrane integrity of the a,b) pristine rGO, c,d) rGO_80MWCNT(10), e,f) rGO_50MWCNT(10), and g,h) GO membranes before and after cross-flow evaluations at different R_e. The black arrows indicate the regions where the integrity of the GO membrane is being compromised.

We believe that this same mechanism can be extended for the nanoarchitectured membranes. Before that, let us recall an important protocol during the processing of the MWCNTs. The MWCNTs have undergone surface functionalization using nitric acid oxidation for 4 h and tip-sonication at 60% amplitude for 1 h prior to membrane fabrication. The strong sonication process not only shortened the lengths of the MWCNTs[33] but at the same time thinned the MWCNTs through exfoliating the oxidized but defective outer walls.[34] Judging from the chemical states of the oxidized MWCNTs (Figure 5b) and the analysis of the TEM images (**Figure 7**a,b), we believe that the observed fragments anchored on the surfaces of the oxidized MWCNTs after tip-sonication are in fact nanoscale GO foliates. Similar observations have also been reported in previous reports.[32,35] As such, we propose that

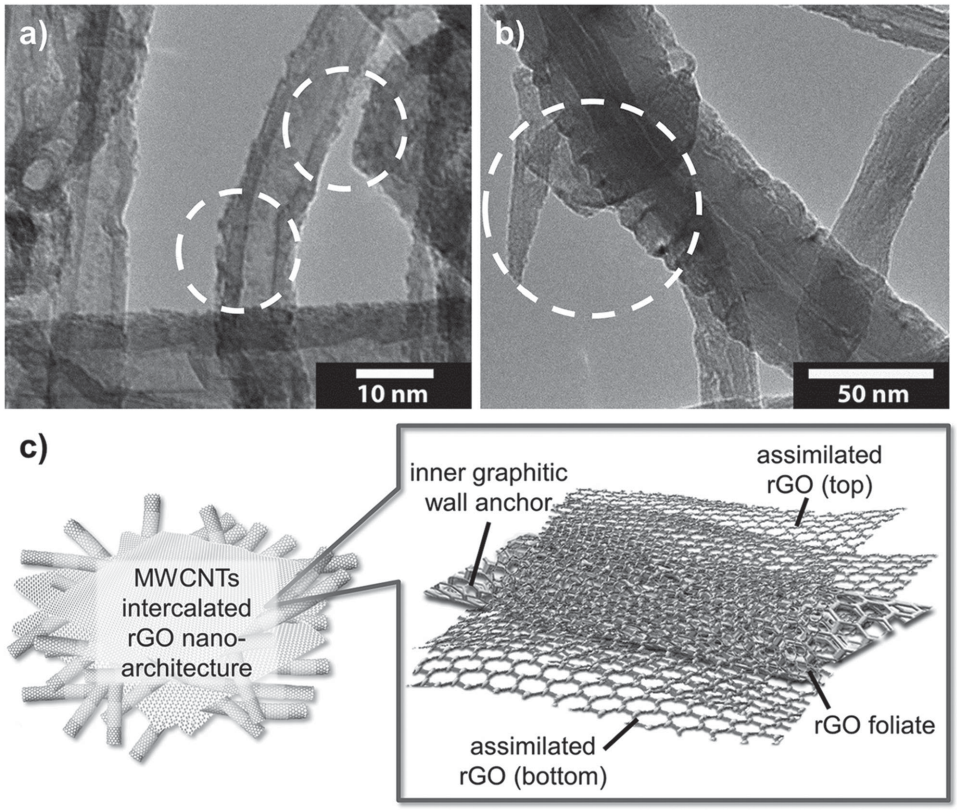

Figure 7. TEM images of the a) 10 nm and b) 50 nm diameter MWCNTs after tip-sonication. The circles in white highlight the presence of rGO foliates. c) Pictorial representation illustrating the van der Waals attractions and π–π stacking interactions between the assimilated rGO sheets and the inner graphitic wall of the MWCNTs via the rGO foliates.

these nanoscale GO foliates on the MWCNTs get reduced into rGO foliates by HI reduction and induce strong van der Waals attractions and π–π stacking interactions[32] between the assimilated rGO sheets and the inner graphitic walls of the MWCNTs (Figure 7c). The excellent stability observed in the nanoarchitectured membranes is a result of such strong interactions.

As an attestation to the above reasoning, 80 wt% single-walled carbon nanotubes (SWCNTs) intercalated rGO membrane was fabricated to study its membrane stability. The same processing protocols were applied on the SWCNTs to ensure an unbiased comparative study. Unsurprisingly, the rGO_80SWCNT membrane did not exhibit the outstanding membrane stability as its rGO_80MWCNT(10) counterpart. The rGO_80SWCNT membrane appears highly porous with water intercalating rapidly into the membrane when exposed to water. Consequently, this causes the membrane to rupture in less than a minute of exposure as captured in Video S3 (Supporting Information). Such an observation provides an important implication concerning the mechanistic understanding of the nanoarchitectured membranes. The intercalated MWCNTs emerge to anchor themselves onto the assimilated rGO sheets through the rGO foliates via strong van der Waals attractions and π–π stacking interactions which is similar to the CNT vein supports as proposed by Lin et al.[35b] and the "rebar graphene" as proposed by Yan et al.[32] Without the support from the inner graphitic walls of the MWCNTs, the nanoarchitecture quickly collapses in water just like in rGO_80SWCNT. In essence, by leveraging on the inner graphitic walls of the MWCNTs as spacers and using the nanoscale rGO foliates to extend toward assimilated rGO sheets via strong interactions, membrane stability can be instilled from within the nanoarchitectured membranes. Such membrane stability is considered superior when compared to those reported in the literature (Table S3, Supporting Information).

Comparing with representative results across the recent literature, rGO_80MWCNT(10) has exhibited comparable water permeability and excellent dye rejection capability. In fact, the water permeability of rGO_80MWCNT(10) is at least twice that of previously reported rGO membranes with similar rejection capabilities (**Table 1**) and five to ten times higher than most commercial NF membranes.[18,36] The superior stability furnished by the pristine rGO and rGO_80MWCNT(10) membranes also offers a greater competitive advantage over other graphene-based membranes with higher water permeability,[37] when it comes to commercial separation applications which utilize cross-flow filtration to mitigate concentration polarization.[38] The membrane stability of such graphene-based membranes is often not reported or generally evaluated in unrepresentative hydrodynamic conditions such as submerging in stagnant water. In comparison, our studies have demonstrated the feasibility of employing nanoarchitectured membranes in cross-flow filtration by engineering the membrane stability through MWCNT intercalation. Considering that the costs of mass producing GO and MWCNTs will continue to drop with

Table 1. Performance and membrane stability of ultrathin pristine rGO and all-carbon nanoarchitectured membranes together with several representative results from recently published works. CCG: chemically converted graphene; PNIPAM: poly(N-isopropylacrylamide); NME: nitrocellulose mixed ester; PC: polycarbonate; CDs: carbon quantum dots (1–3.5 kDa); MCE: mixed cellulose ester; PVDF: polyvinylidene fluoride; DY: direct yellow; EB: evans blue; MO: methyl orange; N.A.: not applicable.

Graphene-based membrane	Fabrication method	Feed system	Water permeability coefficient [$Lm^{-2}\ h^{-1}\ bar^{-1}$]	Rejection [%]	Membrane stability	Ref.
Corrugated CCG	Vacuum filtration	0.01×10^{-3} M DY	45	67	N.A.	[37a]
PNIPAM/CCG (3:1)/NME	Pressure-assisted filtration	RhB	152	70	Stable in water for a month without leakage of PNIPAM	[12c]
GO/PC	Vacuum filtration	15×10^{-6} M EB	71	85	N.A.	[18]
Nanostrand channeled GO/PC	Vacuum filtration	15×10^{-6} M EB	695	83.5	N.A.	[18]
CDs-GO/MCE	Vacuum filtration	10 ppm MB	408–434	99.5	N.A.	[37b]
		10 ppm MO		99.2		
		10 ppm RhB		99.7		
MWCNTs-refluxed GO/PVDF	Vacuum filtration	0.05 g L^{-1} MO	11.33	96.1	Stable under 450 rpm stirring during performance evaluation	[19]
		0.02×10^{-3} M DY		99.8		
Base-refluxed rGO/PVDF	Vacuum filtration	0.02×10^{-3} M MB	21.8	99.2	Stable in water for at least 0.5 year without visible change	[12a]
		0.02×10^{-3} M RhB	5	78		
Ultrathin pristine rGO/PC	Pressure-assisted filtration	0.01 g L^{-1} MB	11	95.2	Stable under 4667 R_e cross-flow evaluation	this work
		0.03×10^{-3} M AO7		95.5		
		0.02×10^{-3} M RhB		97.3		
rGO_80MWCNT (10)/PC	Pressure-assisted filtration	0.01 g L^{-1} MB	52.7	99.8	Stable under 4667 R_e cross-flow evaluation and withstand 1167 R_e cross-flow for at least 24 h	
		0.03×10^{-3} M AO7		99.4		
		0.02×10^{-3} M RhB		100		

the development of better and cheaper scale-up methods,[39] we are confident that our all-carbon nanoarchitectured membranes will be able to find their places in niche separation applications.

3. Conclusion

All-carbon nanoarchitectured membranes were demonstrated with high water permeability, excellent organic dye rejection rates, and superior membrane stability. By loading small diameter MWCNTs (10 nm diameter) in the rGO membranes, the microstructures of the nanoarchitectures can be easily tuned from a graphene-rich type to a CNT-rich type. As a result of this intercalation of MWCNTs, the rGO membrane with 80 wt% MWCNT loading exhibited a water permeability which is 4.8 times higher than that of the pristine rGO membrane. In addition, this membrane provided a better size exclusion effect, with almost 100% rejection rates for three types of organic dyes of different charges. Furthermore, our unprecedented study on the membrane stability has revealed exceptional stability of the all-carbon nanoarchitectured membranes when subjected to a turbulent cross-flow hydrodynamic condition of 2000 mL min^{-1} and Reynolds number of 4667. Mechanistic understanding suggests that the van der Waals attractions and π–π stacking interactions between the assimilated rGO sheets and the nanoscale rGO foliates on the intercalated MWCNT anchors have successfully engineered such membrane stability. These results have demonstrated the effectiveness of our strategy to use MWCNTs as spacers to create nanochannels which selectively facilitate water transport and as anchors to instill the membrane with superior stability for water purification. In general, this nanoarchitecture design is highly versatile in creating both graphene-rich and CNT-rich all-carbon membranes with engineered nanochannels and superior membrane stability for realizing practical separation applications of graphene-based membranes.

4. Experimental Section

Materials: GO was synthesized from graphite powder (Bay Carbon, Michigan) via a modified Hummers and Offeman's method as described in our previous work.[40] The prepared GO solution was then diluted to a stock solution with concentration of 6.5 mg mL^{-1} for membrane fabrication. As received MWCNTs (10 nm: Cnano Technology Ltd. and 50 nm: Cheap Tubes Inc.) and SWCNTs (AP-SWCNT: Carbon Solution Inc.) were first functionalized by refluxing in 69.0% HNO_3 (Sigma-Aldrich) for 4 h. The detailed functionalization procedure can be found in the literature.[33]

Membranes Fabrication: To fabricate the all-carbon nanoarchitectured membranes, a diluted GO solution (0.1 mg mL^{-1}) was first prepared from the stock and subjected to bath-sonication for 30 min to exfoliate the GO. 20 mg of each type of CNTs were dispersed in 100 mL deionized water (DI H_2O) via tip-sonication (Sonics-VCX130) at 5 °C for 1 h to give well-dispersed CNTs solutions (0.2 mg mL^{-1}). These GO and CNTs solutions were immediately used for membrane fabrication after

sonication. 0.222, 0.857, 2, and 4 mL of the MWCNTs (10 nm diameter) solutions were correspondingly added into 4 mL of GO solution and then subjected to pressure-assisted filtration at 1 bar pressure on PC membranes (0.2 um pore size, 47 mm diameter, Millipore) using an in-house made dead-end filtration device to yield membranes containing 10, 30, 50, and 80 wt% MWCNTs, respectively. The same procedure was repeated using MWCNTs (50 nm diameter) to produce 10, 30, 50, and 80 wt% GO_MWCNTs membranes and SWCNTs to produce 80 wt% GO_SWCNTs membrane. To prepare ultrathin GO membrane as a control, 4 mL of the GO solution was likewise filtered without addition of CNTs. The GO loading on all these membranes were kept the same at 0.35 g m^{-2} to ensure the same hydrodynamic resistance from the sheets for comparative studies. The as-prepared membranes were then dried in a drying chamber with temperature and humidity controlled at 35 °C and 40%, respectively, for 24 h. For the preparation of pristine rGO membrane and the nanoarchitectured membranes, the dried membranes were treated with 57 wt% HI (Sigma-Aldrich) vapor at 90 °C for 2–5 min depending on the thickness of the membranes which changed with different wt% of the CNTs added. The reduced membranes were stable to water and thus they were washed with running DI H_2O thrice after the reduction process to remove any excess HI. These cleaned membranes were air-dried and stored under room temperature for evaluation of separation performances.

Evaluations of Separation Performance: The pure water permeability and separation evaluations were performed using an in-house made dead-end filtration device with an applied pressure of 1 bar driven by nitrogen gas. As reported in the literature, the water permeability usually stabilizes after 0.5 to 1 h of compaction.[12a,c] Thus, all of the reported water permeability coefficients of the membranes were obtained after 1 h of compaction in DI H_2O at a pressure of 1 bar. Three different aqueous dye solutions, MB, AO7, and RhB, obtained from Sigma-Aldrich, were utilized to evaluate the membranes separation properties at a pressure of 1 bar. The mean pore diameter and pore size distributions of the membranes were determined using a Levenberg–Marquardt equation and a two-parameter log-normal distribution function as described elsewhere in the literature.[40a,41] The effective membrane area for all these evaluations was 11.34 cm^2. Detailed calculation methods are provided in the Supporting Information.

Characterization: A UV–Vis spectrometer (UV-1800, Shimadzu) was used to quantify the concentrations of the dyes in the retentate, permeate, and feed solutions to obtain the separation performances of the membranes. The membranes surface and cross-sectional morphologies were imaged using a field emission-scanning electron microscope, FE-SEM (JSM-6701F, JEOL), at 5 kV while the morphology and structural integrity of the MWCNTs were characterized using a transmission electron microscope, TEM (JEM-1400, JEOL), at 80 kV. The surface morphology, roughness, height profile of the GO and pristine rGO membranes, and the lateral dimensions of the GO sheets (Figure S9, Supporting Information) were also elucidated via atomic force microscopy, AFM (MFP-3D, Asylum Research) in the AC mode. An attenuated total reflection Fourier transformed-infrared, ATR FT-IR (IR Prestige-21, Shimadzu) spectrometer was employed to study the surface functional groups of the membranes and the MWCNTs before and after reduction. The microstructural integrity of the membranes was investigated using Raman spectroscopy (Renishaw) equipped with a 785 nm laser source while the XRD patterns of the membranes in wet and dry states were obtained using an X-ray diffractometer (D2 Phaser, Bruker) equipped with a Cu K_α radiation source. A goniometer (OCA, DataPhysics, GmbH) was used to measure the water contact angles of the membranes before and after reduction.

Membrane Stability Evaluation: Membrane stability was studied under various cross-flow rates using an in-house made membrane cross-flow testing cell. A peristaltic pump (Masterflex L/S, Cole Parmer) was utilized to pump DI H_2O into the cell at a cross-flow rate ranging from 40 to 2000 mL min^{-1}. The pristine rGO and nanoarchitectured membranes were initially subjected 40 mL min^{-1} cross-flow rate before the rates were increased to 500, 1000, and 2000 mL min^{-1} for a duration of 10 min at every rate. For the GO membrane, the highest cross-flow rate evaluated was 500 mL min^{-1}. These cross-flow rates were quantified into Reynolds number, R_e (see the Supporting Information), to assess membrane stability under different flow conditions. The effective membrane area for these stability evaluations was 4.5 cm^2.

Supporting Information

Supporting Information is available from the Wiley Online Library or from the author.

Acknowledgements

This work was supported by the Ministry of Education, Singapore (MOE2011-T2-2-062 and 2013-T1-002-132), iFood program funded by Nanyang Technological University, Singapore, the Youth 1000 Talent Program of China, and the National Natural Science Foundation of China (No. 51233008). The authors would also like to thank funding support from the Singapore Economic Development Board to Singapore Membrane Technology Center.

Received: July 16, 2015
Revised: September 18, 2015
Published online: November 6, 2015

[1] a) M. A. Shannon, P. W. Bohn, M. Elimelech, J. G. Georgiadis, B. J. Marinas, A. M. Mayes, *Nature* **2008**, *452*, 301; b) M. Elimelech, W. A. Phillip, *Science* **2011**, *333*, 712; c) T. Hillie, M. Hlophe, *Nat. Nanotechnol.* **2007**, *2*, 663.
[2] D. L. Gin, R. D. Noble, *Science* **2011**, *332*, 674.
[3] a) G. Liu, W. Jin, N. Xu, *Chem. Soc. Rev.* **2015**; b) A. J. Brown, N. A. Brunelli, K. Eum, F. Rashidi, J. R. Johnson, W. J. Koros, C. W. Jones, S. Nair, *Science* **2014**, *345*, 72.
[4] a) F. Du, L. Qu, Z. Xia, L. Feng, L. Dai, *Langmuir* **2011**, *27*, 8437; b) B. Lee, Y. Baek, M. Lee, D. H. Jeong, H. H. Lee, J. Yoon, Y. H. Kim, *Nat. Commun.* **2015**, *6*, 7109; c) R. R. Nair, H. A. Wu, P. N. Jayaram, I. V. Grigorieva, A. K. Geim, *Science* **2012**, *335*, 442.
[5] a) B. J. Hinds, *Science* **2004**, *303*, 62; b) J. K. Holt, H. G. Park, Y. M. Wang, M. Stadermann, A. b. Artyukhin, C. P. Grigoropoulos, A. Noy, O. Bakajin, *Science* **2006**, *312*, 1034; c) H. Li, Z. Song, X. Zhang, Y. Huang, S. Li, Y. Mao, H. J. Ploehn, Y. Bao, M. Yu, *Science* **2013**, *342*, 95; d) K. Huang, G. Liu, Y. Lou, Z. Dong, J. Shen, W. Jin, *Angew. Chem. Int. Ed.* **2014**, *53*, 6929; e) J. Shen, G. Liu, K. Huang, W. Jin, K.-R. Lee, N. Xu, *Angew. Chem., Int. Ed.* **2015**, *54*, 578.
[6] a) G. Algara-Siller, O. Lehtinen, F. C. Wang, R. R. Nair, U. Kaiser, H. A. Wu, A. K. Geim, I. V. Grigorieva, *Nature* **2015**, *519*, 443; b) S. P. Surwade, S. N. Smirnov, I. V. Vlassiouk, R. R. Unocic, G. M. Veith, S. Dai, S. M. Mahurin, *Nat. Nanotechnol.* **2015**, *10*, 459; c) S. C. O'Hern, M. S. H. Boutilier, J.-C. Idrobo, Y. Song, J. Kong, T. Laoui, M. Atieh, R. Karnik, *Nano Lett.* **2014**, *14*, 1234.
[7] a) S. Stankovich, D. A. Dikin, O. C. Compton, G. H. B. Dommett, R. S. Ruoff, S. T. Nguyen, *Chem. Mater.* **2010**, *22*, 4153; b) S. Sun, C. Wang, M. Chen, M. Li, *Chem. Phys. Lett.* **2013**, *561–562*, 166.
[8] L. Huang, Y. Li, Q. Zhou, W. Yuan, G. Shi, *Adv. Mater.* **2015**, *27*, 3797.
[9] H. Liu, H. Wang, X. Zhang, *Adv. Mater.* **2015**, *27*, 249.
[10] Y. Su, V. G. Kravets, S. L. Wong, J. Waters, A. K. Geim, R. R. Nair, *Nat. Commun.* **2014**, *5*, 4843.
[11] C.-N. Yeh, K. Raidongia, J. Shao, Q.-H. Yang, J. Huang, *Nat. Chem.* **2015**, *7*, 166.

[12] a) Y. Han, Z. Xu, C. Gao, *Adv. Funct. Mater.* **2013**, *23*, 3693; b) Y. Liu, J. H. Dustin Lee, Q. Xia, Y. Ma, Y. Yu, L. Yung, J. Xie, C. N. Ong, C. D. Vecitis, Z. Zhou, *J. Mater. Chem. A* **2014**, *2*, 16554; c) Y. Wang, S. Chen, L. Qiu, K. Wang, H. Wang, G. P. Simon, D. Li, *Adv. Funct. Mater.* **2014**, *25*, 126.
[13] C.-H. Tsou, Q.-F. An, S.-C. Lo, M. De Guzman, W.-S. Hung, C.-C. Hu, K.-R. Lee, J.-Y. Lai, *J. Membr. Sci.* **2015**, *477*, 93.
[14] a) A. Noy, H. G. Park, F. Fornasiero, J. K. Holt, C. P. Grigoropoulos, O. Bakajin, *Nano Today* **2007**, *2*, 22; b) R. Lv, E. Cruz-Silva, M. Terrones, *ACS Nano* **2014**, *8*, 4061.
[15] L. J. Cote, J. Kim, Z. Zhang, C. Sun, J. Huang, *Soft Matter* **2010**, *6*, 6096.
[16] Ch. Laurent, E. Flahaut, A. Peigney, *Carbon* **2010**, *48*, 2994.
[17] X. Zhao, X. Bu, T. Wu, S.-T. Zheng, L. Wang, P. Feng, *Nat. Commun.* **2013**, *4*, 2344.
[18] H. Huang, Z. Song, N. Wei, L. Shi, Y. Mao, Y. Ying, L. Sun, Z. Xu, X. Peng, *Nat. Commun.*, **2013**, *4*, 2979.
[19] Y. Han, Y. Jiang, C. Gao, *ACS Appl. Mater. Interfaces* **2015**, *7*, 8147.
[20] a) S. Pei, J. Zhao, J. Du, W. Ren, H.-M. Cheng, *Carbon* **2010**, *48*, 4466; b) A. C. Ferrari, J. Robertson, *Phys. Rev. B* **2000**, *61*, 14095.
[21] M. S. Dresselhaus, A. Jorio, M. Hofmann, G. Dresselhaus, R. Saito, *Nano Lett.* **2010**, *10*, 751.
[22] K. Krishnamoorthy, M. Veerapandian, K. Yun, S.-J. Kim, *Carbon* **2013**, *53*, 38.
[23] A. M. Craig, Introduction to IR Spectra, http://www.chem.ucla.edu/~webspectra/irintro.html (accessed: July 2015).
[24] W.-S. Hung, C.-H. Tsou, M. D. Guzman, Q.-F. An, Y.-L. Liu, Y.-M. Zhang, C.-C. Hu, K.-R. Lee, J.-Y. Lai, *Chem. Mater.* **2014**, *26*, 2983.
[25] S. Park, J. An, J. R. Potts, A. Velamakanni, S. Murali, R. S. Ruoff, *Carbon* **2011**, *49*, 3019.
[26] K. Zhang, Y. Zhang, S. Wang, *Sci. Rep.* **2013**, *3*, 3448.
[27] D. Yu, Y. Chen, B. Li, X. Chen, M. Zhang, *Appl. Phys. Lett.* **2007**, *90*, 161103.
[28] a) D. Li, M. B. Muller, S. Gilje, R. B. Kaner, G. G. Wallace, *Nat. Nanotechnol.* **2008**, *3*, 101; b) B. Konkena, S. Vasudevan, *J. Phys. Chem. Lett.* **2012**, *3*, 867.
[29] a) R. K. Joshi, P. Carbone, F. C. Wang, V. G. Kravets, Y. Su, I. V. Grigorieva, H. A. Wu, A. K. Geim, R. R. Nair, *Science* **2014**, *343*, 752; b) B. Mi, *Science* **2014**, *343*, 740.
[30] X.-L. Wang, W.-J. Shang, D.-X. Wang, L. Wu, C.-H. Tu, *Desalination* **2009**, *236*, 316.
[31] N. F. D. Aba, J. Y. Chong, B. Wang, C. Mattevi, K. Li, *J. Membr. Sci.* **2015**, *484*, 87.
[32] Z. Yan, Z. Peng, G. Casillas, J. Lin, C. Xiang, H. Zhou, Y. Yang, G. Ruan, A.-R. O. Raji, E. L. G. Samuel, R. H. Hauge, M. J. Yacaman, J. M. Tour, *ACS Nano* **2014**, *8*, 5061.
[33] K. Goh, L. Setiawan, L. Wei, W. Jiang, R. Wang, Y. Chen, *J. Membr. Sci.* **2013**, *446*, 244.
[34] I. D. Rosca, F. Watari, M. Uo, T. Akasaka, *Carbon* **2005**, *43*, 3124.
[35] a) D. V. Kosynkin, A. L. Higginbotham, A. Sinitskii, J. R. Lomeda, A. Dimiev, B. K. Price, J. M. Tour, *Nature* **2009**, *458*, 872; b) X. Lin, P. Liu, Y. Wei, Q. Li, J. Wang, Y. Wu, C. Feng, L. Zhang, S. Fan, K. Jiang, *Nat. Commun.* **2013**, *4*, 2920; c) Y. Li, W. Zhou, H. Wang, L. Xie, Y. Liang, F. Wei, J.-C. Idrobo, S. J. Pennycook, H. Dai, *Nat. Nanotechnol.* **2012**, *7*, 394.
[36] M. Hu, B. Mi, *Environ. Sci. Technol.* **2013**, *47*, 3715.
[37] a) Q. Ling, X. H. Zhang, W. R. Yang, Y. F. Wang, G. P. Simon, D. Li, *Chem. Commun.* **2011**, *47*, 5810; b) W. Wang, E. Eftekhari, G. Zhu, X. Zhang, Z. Yan, Q. Li, *Chem. Commun.* **2014**, *50*, 13089.
[38] T. Cath, A. Childress, M. Elimelech, *J. Membr. Sci.* **2006**, *281*, 70.
[39] Q. Zhang, J.-Q. Huang, M.-Q. Zhao, W.-Z. Qian, F. Wei, *ChemSusChem* **2011**, *4*, 864.
[40] a) K. Goh, L. Setiawan, L. Wei, R. Si, A. G. Fane, R. Wang, Y. Chen, *J. Membr. Sci.* **2015**, *474*, 244. b) W. S. Hummers, R. E. Offeman, *J. Am. Chem. Soc.* **1958**, *80*, 1339.
[41] a) J. Ren, R. Wang, H.-Y. Zhang, Z. Li, D. T. Liang, J. H. Tay, *J. Membr. Sci.* **2006**, *281*, 334. b) J. Ren, Z. Li, F.-S. Wong, *J. Membr. Sci.* **2006**, *279*, 558.